Observation of a Prethermal $U(1)$ Discrete Time Crystal

Andrew Stasiuk[1,*] and Paola Cappellaro[1,2]
[1]*Department of Nuclear Science and Engineering, Massachusetts Institute of Technology,*
Cambridge, Massachusetts 02139, USA
and Research Laboratory of Electronics, Massachusetts Institute of Technology,
Cambridge, Massachusetts 02139, USA
[2]*Department of Physics, Massachusetts Institute of Technology, Cambridge, Massachusetts 02139, USA*

(Received 29 March 2023; revised 20 July 2023; accepted 8 September 2023; published 26 October 2023)

A time crystal is a state of periodically driven matter that breaks discrete time-translation symmetry. Time crystals have been demonstrated experimentally in various programmable quantum simulators, and they exemplify how nonequilibrium, driven quantum systems can exhibit intriguing and robust properties absent in systems at equilibrium. These robust driven states need to be stabilized by some mechanism, with the preeminent candidates being many-body localization and prethermalization. This introduces additional constraints that make it challenging to experimentally observe time crystallinity in naturally occurring systems. Recent theoretical work has developed the notion of prethermalization *without temperature*, expanding the class of time-crystal systems to explain time-crystalline observations at (or near) infinite temperature. In this work, we conclusively observe the emergence of a prethermal $U(1)$ time-crystalline state at quasi-infinite temperature in a solid-state NMR quantum emulator by verifying the requisites of prethermalization without temperature. In addition to observing the signature period-doubling behavior, we show the existence of a long-lived prethermal regime whose lifetime is significantly enhanced by strengthening an emergent $U(1)$ conservation law. Not only do we measure this enhancement through the global magnetization, but we also exploit on-site disorder to measure local observables, ruling out the possibility of many-body localization and confirming the emergence of long-range correlations.

DOI: 10.1103/PhysRevX.13.041016

Subject Areas: Condensed Matter Physics,
Quantum Information,
Strongly Correlated Materials

I. INTRODUCTION

The proposal for the existence of time crystals posited that there exist systems that might break discrete time-translation symmetry [1], in analogy to spatial symmetry breaking in conventional crystals. However, it was quickly shown that such a feat is impossible for quantum systems at equilibrium [2]. In out-of-equilibrium systems, however, there is no fundamental restriction forbidding the emergence of time-crystalline order [3].

Specifically, in periodically driven, many-body quantum systems, it has been demonstrated that there exist long-lived states of matter that break discrete time-translation symmetry [3]. To engineer such robust driven states, there must be a mechanism to prevent Floquet heating so as to avoid driving the system to infinite temperature. For a closed quantum system with disorder, many-body localization (MBL) is sufficient to prevent Floquet heating [4]. Thus, early experiments sought to use this phenomenon, though doubts have been cast on initial attempts at observing MBL discrete time crystals (DTCs) in an ion-trap quantum simulator due to the system's dimensionality. Recently, there have been more conclusive observations of discrete time crystals stabilized by MBL in superconducting qubit processors [5,6]. However, the phenomenon of MBL is hard to achieve experimentally as it requires both strong disorder and short-range interactions. Such stringent conditions make the MBL DTCs difficult to realize experimentally [7].

Instead of MBL, a different mechanism to avoid Floquet heating can be pursued, namely, the phenomenon of prethermalization [8]. In particular, prethermal quantum systems exhibit lifetimes that are exponential in the Floquet driving frequency, without the need for any source of disorder [9,10]. However, prethermal time crystals require long-range interactions and low temperatures to meaningfully induce spontaneous symmetry breaking (SSB) [3]. Prethermal discrete time crystals (PDTC) have also been experimentally observed in

---

[*] astasiuk@mit.edu

quantum systems with high purity initial states due to low temperatures or hyperpolarization [11–13].

As the explorations into out-of-equilibrium quantum systems have matured, many experimental platforms have demonstrated the emergence of time-crystalline signatures under periodic driving. In addition to observations in small-scale simulators such as ion traps [11] and superconducting qubits [13], time-crystalline order has been observed in large-scale devices such as dipolar NV ensembles [12,14] and solid-state NMR systems [15,16] (see Ref. [17] for a more complete list of recent theoretical and experimental progress across various systems).

In the case of NMR and other high-entropy simulators, there has been some confusion as to the cause of the observed emergent time-crystalline state, as the system was at too high a temperature to exhibit the effects of spontaneous symmetry breaking and not disordered enough to be stabilized by MBL [15–17]. However, recent work has shown that a third type of time crystal is possible, a prethermal $U(1)$ time crystal, allowing for prethermalization *without* temperature [18]. It is likely that some previous high-temperature studies of time crystallinity have been instances of prethermal $U(1)$ DTCs. However, verification of this fact requires the measurement of local observables previously thought to be inaccessible in NMR and other large-scale systems restricted to global control [18]. Furthermore, there are theoretical proposals for additional stabilization mechanisms, such as mesonic domain-wall confinement, which may be applicable in intermediate-temperature systems [19].

In this work, we drive a macroscopic solid-state NMR system [20] to engineer time crystallinity and verify that we observe a prethermal $U(1)$ time crystal by comparing local to global observables. In particular, we utilize a recently developed technique to leverage on-site disorder to measure spatially averaged, truly local observables in large quantum ensembles without universal or single-site control [21,22].

II. METHODS

Our system is a quasi-1D nuclear spin ensemble. This is achieved experimentally using a single-crystal sample of fluorapatite. The crystal structure of fluorapatite is given in Fig. 1.

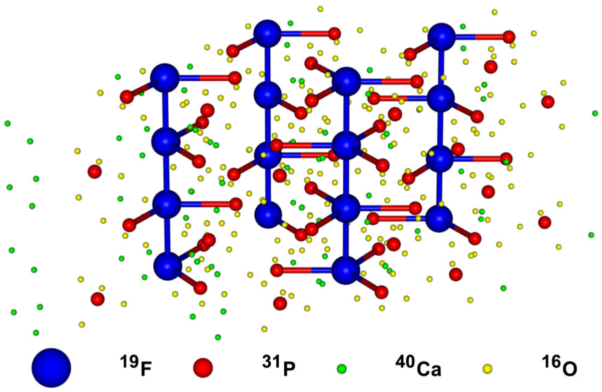

FIG. 1. Crystal structure of fluorapatite, $\mathrm{Ca_5(PO_4)_3F}$, with an emphasis on the spin-full nuclei. Intrachain fluorine (blue) bonds and nearest-neighbor fluorine-phosphorus (blue-red) bonds are shown. Additionally, the spin-less nuclei of oxygen (yellow) and calcium (green) are included with no bonds shown. The spin-full isotopes of calcium and oxygen are less than 1% natural abundance and neglected. The vertical crystal c-axis length is 6.805 Å (with two ^{19}F per unit cell), while the horizontal a, b axes are 9.224 Å long [23].

The crystal is placed in a large (about 7.1 T) magnetic field aligned along the crystal's c axis, so the intrachain coupling is approximately 40 times larger than the interchain coupling [24]. Within the rotating frame generated by the magnetic field, our system Hamiltonian has three main components: dipolar z, locally disordered z, and collective control.

$$\mathcal{H}(t) = \mathcal{H}_{Dz} + \mathcal{H}_{\mathrm{dis}} + \mathcal{H}_c(t). \tag{1}$$

Concretely, each component of the Hamiltonian is as follows:

$$\mathcal{H}_{Dz} = \frac{1}{2}\sum_{i<j} J_{ij}\left(\hat{S}_z^{(i)}\hat{S}_z^{(j)} - \frac{1}{2}\left(\hat{S}_x^{(i)}\hat{S}_x^{(j)} + \hat{S}_y^{(i)}\hat{S}_y^{(j)}\right)\right),$$

$$\mathcal{H}_{\mathrm{dis}} = \sum_i \omega_i \hat{S}_z^{(i)},$$

$$\mathcal{H}_c(t) = f(t)\big(\cos(\phi)\hat{S}_x + \sin(\phi)\hat{S}_y\big),$$

where $J_{ij} = J_0/|i-j|^3$ ($J_0 = 32.843\ \mathrm{krad\,s^{-1}}$), and we have defined the global magnetization operators

$$\hat{S}_\nu = \frac{1}{2}\sum_i \hat{\sigma}_\nu^{(i)}, \qquad \nu \in \{x, y, z\}. \tag{2}$$

The locally disordered field arises from the heteronuclear interaction of the fluorine and phosphorus spins. Finally, the collective control drive can be amplitude modulated via the function $f(t)$ to produce square pulses of length 1.02 μs resulting in $\pi/2$ rotations, with a minimum interpulse delay of 2.5 μs. The transverse rotation axis is determined by the phase ϕ, which has a resolution of 1 degree. Then, arbitrary x- and y-axis rotations are performed using the following decomposition,

$$R_y(\theta) = R_y(-\pi/2)R_z(\theta)R_y(\pi/2). \tag{3}$$

Note that z-axis rotations of an angle θ are performed by phase shifting all subsequent pulses by the same angle, θ, called virtual-z gates [25,26].

As is standard in NMR, our initial state is well represented by the reduced density matrix $\delta\rho(0) = \hat{S}_z$. As the main observable of interest is also the magnetization along the z axis, we can write the signal as an infinite-temperature two-point correlator,

$$m_z(t) = \mathrm{tr}(\hat{\rho}(t)\hat{S}_z) \approx \mathrm{tr}(\delta\hat{\rho}(t)\hat{S}_z) = \langle \hat{S}_z(t)\hat{S}_z \rangle_{\beta=0}. \tag{4}$$

By exploiting the dephasing induced by the disordered field, we can also generate states and observables that provide access to local correlations [21]. By use of spectral sequences [27,28], we turn off the dipolar interactions while leaving the disordered field on, so spin i locally evolves under the Hamiltonian $\omega_i \hat{S}_z^{(i)}$ for a time τ_d. After phase cycling, we are left with a state of the form

$$\delta\hat{\rho} = \sum_i \xi_i \hat{S}_z^{(i)}, \tag{5}$$

where $\xi_i = \sin(\omega_i \tau_d)$ are independent and identically distributed random variables with zero mean. Importantly, we have previously shown that $\mathbb{E}[\xi_i \xi_j] \approx \delta_{ij}$, where $\mathbb{E}$ denotes the spatiotemporal expectation value of the random variables [21].

In order to demonstrate a $U(1)$ DTC, we engineer the simplest periodic sequence that can display such behavior. We alternate between a collective rotation, $R_\nu(\theta) = e^{i\theta\hat{S}_\nu}$, and evolution under a Hamiltonian $\mathcal{H}_D$ (which might be obtained via Floquet Hamiltonian engineering, as described below) for a time T (which is thus the Floquet and DTC period). We often refer to the combination of these two steps as evolution with periodic kicking, in analogy to pushing a swing. Without loss of generality, to vary the effective kicking frequency $\omega \sim 1/T$, we can either vary the interaction time between kicks or vary the interaction strength of $\mathcal{H}_D$ between equally spaced kicks. To this effect, we consider variations of the dimensionless interaction magnitude, defined as

$$\gamma = J_{\mathrm{eff}}/\omega = uT_0 J_0, \qquad u \geq 0. \tag{6}$$

In Eq. (6), γ can be varied either by changing the evolution time $T = uT_0$ (Sec. III A) or by using Hamiltonian engineering sequences (Wei16 and Peng24 in Sec. III B) to vary $J_{\mathrm{eff}} = uJ_0$ while keeping the evolution time (here, $T_0 = 120$ μs) fixed. Given $J_0 T_0 = 3.94$ radians, $\gamma = 1.25\pi u$.

We utilize the control to perform high-fidelity Floquet engineering sequences such as Wei16 [29], which allows for rescaling the spin-spin interactions [30], and the Peng24 time-suspension sequence [31], which aims at canceling the whole Hamiltonian. To illustrate this technique, and the fidelity of our control, we perform repeated $\theta = \pi$ and $(1-2\epsilon)\pi$ kicking on an effectively noninteracting ensemble of nuclear spins, $\mathcal{H}_D = 0$. This is achieved using the Peng24 time-suspension sequence, which decouples interactions over a $T = 120$ μs Floquet period [31]. As shown in Fig. 2, the noninteracting decay envelope closely fits a stretched exponential model, given in Eq. (7),

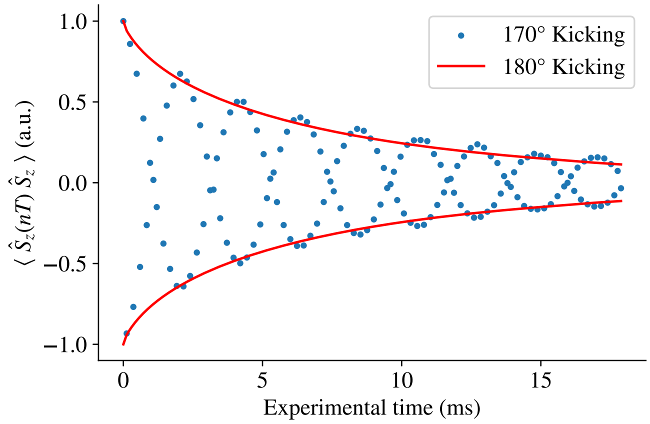

FIG. 2. Magnetization of noninteracting spin ensembles under repeated kicking. Each Floquet cycle is $T = 120$ μs long, comprising evolution under the time-suspension sequence followed by an $R_y(\theta)$ unitary, with $\theta \in \{170, 180\}$ degrees. Perfect π kicking gives trivial period doubling, with a stretched exponential ($b = 0.70$) decay with a timescale of $\tau \approx 6.573$ ms [Eq. (7), $a \approx 1$, $c \approx 0$]. The $\theta = (1-2\epsilon)\pi$ kicking results in beating with a frequency of $\frac{1}{2} \pm \epsilon$ decaying on a similar timescale.

$$S(t) \equiv \langle \hat{S}_z(t)\hat{S}_z \rangle = a \exp\left(-(t/\tau)^b\right) + c. \tag{7}$$

The long-lived signal ($\tau \approx 6573$ μs, compared to a free induction decay time of approximately 30 μs) and precise beating frequency confirm that the compiled pulse technique can perform an arbitrary, high-fidelity rotation in conjunction with a Hamiltonian engineering sequence.

III. RESULTS

We explore our system's ability to exhibit time crystallinity using a variety of techniques. First, we vary the effective Floquet period via two physical implementations to evaluate the robustness of our control scheme. Further, in an effort to distinguish between trivial and nontrivial period doubling, we demonstrate our ability to generate robust period doubling as a function of the deviation from perfect π kicking, ϵ. To that end, we show the emergence of a long-lived prethermal regime near the period-doubling phase boundary. Finally, we conclusively diagnose our system as a prethermal $U(1)$ time crystal by showing its insensitivity to disordered fields and the rapid decay of local observables without beating. Given this diagnosis, we enhance $U(1)$ conservation by adding a stroboscopic z field and demonstrate a significant lengthening of the prethermal timescale.

A. Variable interaction time

To explore the large $\gamma > (5/16)\pi$ ($u > 0.25$) regime, we particularize to $\theta = 170°$ and repeatedly drive the system with variable physical delay $T = uT_0$ between kicks.

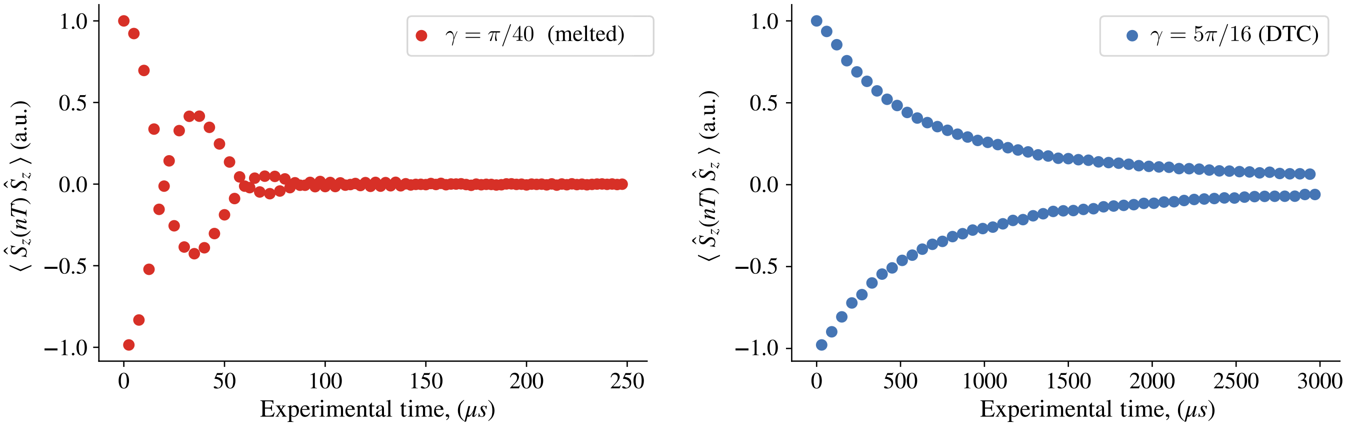

FIG. 3. Time traces of the magnetization response for noncrystalline (left panel) and time-crystalline (right panel) systems under $\theta = 170°$ driving. The interaction strength is set by the physical interaction time, $T = uT_0$. Notice the dramatic order-of-magnitude improvement in signal lifetime of the time crystal over the melted crystal.

In other words, γ is varied by physically varying the driving period. Here, $\mathcal{H}_D = \mathcal{H}_{Dz}$ is generated by the natural system Hamiltonian, so there are no Trotter errors. At large values of γ, equivalent to a low driving frequency here, we find that the four-parameter model given in Eq. (7) remains a good fit. The decay is close to a simple exponential, with the exponential parameter b nearly unity, taking values between 0.92 and 0.94 for select values of $\gamma \in [(5/16)\pi, (5/4)\pi]$. This indicates that the emergence of period doubling in this regime is a decoherence-dominated effect.

Importantly, we notice that the decay timescale as a function of γ, $\tau(\gamma)$, is linear with a positive slope. By changing to nondimensional units, this linear trend implies that the nondimensional decay constant $\tau_F = \tau/T$ is bounded above by about 37 Floquet periods. This provides additional evidence that the increase in signal lifetime with increasing γ (decreasing driving frequency) is not a time-crystalline effect. Indeed, time crystals have lifetimes that can be generically enhanced by increasing the interaction strength. Thus, we determined that the period-doubling signature for $\gamma > (5/16)\pi$ is trivial and not time crystalline. Explicit details of this analysis are provided in Appendix C.

In the small $\gamma < (5/16)\pi$ regime ($u \in (0, 0.25]$), we find a transition between beating and period-doubled responses. Near the boundary of the transition, there is a breakdown in the fitting of the envelope to a single exponential. The departure from stretched exponential behavior is good evidence that this period doubling is not a decoherence effect; rather, it is evidence of a genuine time crystal. The real-time responses of a time crystal and a melted crystal are shown in Fig. 3. In Fig. 4, we demonstrate our ability to induce period doubling in the magnetization signal by increasing γ, an oft-cited hallmark of time crystallinity. Further, in the small γ regime where either beating or period doubling occurs, we find that the single exponential model is a bad fit for the signal's decay. In fact, when the observed signal $m_z(t)$ is transformed to $-\log|m_z(t)|$, it becomes evident that there are two exponential timescales present. We see a short and rapid decay followed by a much slower decay rate—strong evidence for prethermalization and genuine time crystallinity. In fact, the slow decay rate of the prethermal state is expected to be exponentially suppressed by increasing the driving frequency [3,11,18,32]. Details of this fitting can be found in Appendix C.

In the current implementation, the accessible driving frequencies are experimentally limited. Indeed, we note that the $(1 - 2\epsilon)\pi$ pulse takes approximately 4.5 μs to perform. In other words, the effective pulse length is

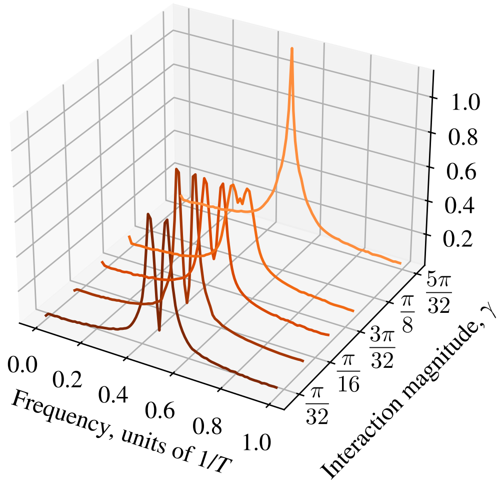

FIG. 4. Fourier transform of the magnetization signal, $\mathcal{F}(m_z(t))$, for various interaction magnitudes $\gamma = uJ_0T_0$ under 170° kicking. The interaction magnitude is set by physically varying the time between consecutive $R_y(\theta)$ unitary kicks. For small γ, the signals show beating consistent with the $\theta \neq \pi$ drive. At large enough γ ($\gamma > \pi/8$), the beating is replaced with a single "period-doubled" peak, often taken to herald a system's transformation to a time crystal.

longer than the interaction time of the smallest considered γ, $\gamma = \pi/40$ ($T = uT_0 = 2.5\ \mu\mathrm{s}$). The interaction Hamiltonian during the drive can be a possible source of confounding error, especially for small γ, where the driving period uT_0 is on the order of the pulse length. We eliminate this source of confounding error in the next section by fixing T and varying the effective interaction strength, $J = uJ_0$, directly.

B. Variable interaction strength

To reduce the effect of the finite pulse width, we now utilize Hamiltonian engineering to fix the interaction time $T = T_0$ and vary the interaction strength $J_{\mathrm{eff}} = uJ_0$. This allows for higher resolution and control in the interaction magnitude γ and is expected to reduce error sources for small γ experiments. The range of interaction magnitudes allowed by Wei16 is limited and cannot achieve large values of γ; namely, $\gamma \geq (5/12)\pi$ is forbidden. The large γ regime is well analyzed in the previous section, and in this section, we intend to particularize only to the small γ regime.

By varying the interaction magnitude γ and the kicking angle $\theta = (1 - 2\epsilon)\pi$, we can estimate the boundary between signals displaying time-translation symmetry breaking (TTSB) and trivial beating. To do so, we take the discrete Fourier transform of the measured signal. Given our signal $S(nT)$, for $n = 0, 1, \ldots, N-1$, the Fourier signal is given by

$$P(k) = \frac{1}{\sqrt{N}} \sum_{n=0}^{N-1} S(nT) e^{-\mathrm{i}\frac{2\pi k n}{N}}, \tag{8}$$

where $k \in \{0, 1, \ldots, N-1\}$. We find the existence of two main structures in the Fourier signal (Fig. 4): a peak at $f = \frac{1}{2}$, $P_{1/2} = |P(N/2)|$, and a pair of peaks at $f = \frac{1}{2} \pm \epsilon$, $P_\epsilon = |P(N/2 \pm N\epsilon)|$. Then, to estimate the transition boundary, we consider the difference $P_{1/2} - P_\epsilon$. The values of this metric are plotted in Fig. 5 for various values of γ and ϵ. Notably, the boundary curve corresponding to $P_{1/2} - P_\epsilon = 0$ is linear in ϵ and γ, plotted as a dashed black line.

Using this metric, we experimentally determine a "phase boundary" between a TTSB and a beating magnetization signal, as done previously [33,34]. In light of recent analyses of time crystallinity in NMR systems, this metric is insufficient to conclusively characterize time crystallinity [17]. However, we can conclude that below the fitted boundary line at $P_{1/2} - P_\epsilon = 0$, beating is dominant, and thus the observed behavior is not time crystalline. Instead, in the blue regions above the boundary line, Fig. 5 simply indicates that the observed signal *might be* time crystalline.

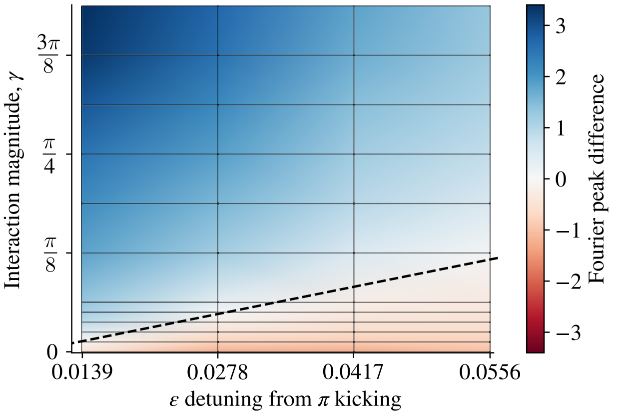

FIG. 5. Difference in selected Fourier peak magnitudes of the observed magnetization under variable interaction magnitude (γ) and deviation from perfect π kicking (ϵ). Blue (red) shaded regions indicate a larger (smaller) period-doubled response than beating. Experimental data were collected for points at vertices of the grid lines; peak differences are smoothed within each grid for easier visualization. Using smoothed interpolations of the data, we estimate the intersection of beating and period doubling for each instance of ϵ. The resulting intersections lead to the fitted phase boundary, shown as a dashed black line.

As discussed in Sec. III A, an interaction magnitude that is too large results in a trivial exponential decay, and thus, it is not genuinely time crystalline. Further, we have carefully verified that an interaction magnitude that is too small also fails to be time crystalline. We expect, then, that genuine long-lived time crystals should emerge just past the crystallization boundary. In this regime, we expect to see a prethermal lifetime that is exponential in the driving frequency [17,18,20]. Namely, once prethermalization has occurred, we expect to find a significant increase in any present decay timescale. In the remaining sections, we will focus on analyzing the period-doubled region of the phase diagram and argue that, near the boundary, we observe prethermalization and hence genuine time crystallinity.

It has previously been argued that at infinite temperature, and in short-range interacting 1D systems, spontaneous-symmetry-breaking (SSB) prethermal discrete time crystals are forbidden [3,8,17]. In this section, we have demonstrated compelling evidence to support the observation of a prethermal $U(1)$ time crystal, which is robust and long-lived even in a quasi-1D system at an effective infinite temperature [18]. In the following sections, we verify that this is indeed the case by enhancing the prethermal lifetime and conclusively ruling out MBL.

C. Behavior of spatiotemporal correlations

Further verification of time crystallinity and $U(1)$ prethermalization requires exploration of additional observables, as emphasized by Luitz *et al.* [18]. In particular, the emergent $U(1)$ conservation law is *global*. In other words, our prethermal Hamiltonian conserves global, also called "collective," magnetization but not local magnetization. This phenomenon has previously been understood in the context of spin diffusion in solid lattices, wherein, initially, local magnetization is transported through the lattice [35,36]. In contrast, if the emergent time-crystalline behavior was induced via MBL, then instead of global $U(1)$ conservation, we should find an extensive number of local integrals of motion (LIOMs) [37,38]. Then, LIOMs will either conserve local magnetization or the local magnetization will oscillate between states of overlapping LIOMs [39]. By suppressing the effects of disorder during Floquet engineering, we *a priori* do not expect to find the emergence of MBL. However, given the presence of disordered fields in our system, we will verify that no localization emerges.

The Wei16 engineering sequence, in addition to providing variable interaction magnitude in fixed time, allows us to modulate the strength of the disorder induced by nearby unpolarized phosphorus spins by varying the efficiency of refocusing the interaction. We exploited this capability to find no significant difference in the global magnetization's response to periodic driving from no disorder up to the maximum allowable disorder under Wei16 (see Fig. 12 in Appendix F). This alone may be sufficient evidence to suggest that many-body localization is not occurring. However, there may be additional sources of disorder, such as drive field inhomogeneity, which reside outside of our primary model [15]. To conclusively rule out MBL as the source of time crystallinity, we utilize on-site disorder to produce a randomly polarized state (and observable), given by Eq. (5). The procedure to create such a state and observable was developed on this system and previously verified [20,21]. In particular, we measure truly local magnetization with an observable signal of the form

$$S_{\mathrm{loc}}(t) = \sum_i \left\langle \hat{\sigma}_z^{(i)}(t)\hat{\sigma}_z^{(i)} \right\rangle_{\beta=0}. \tag{9}$$

In Fig. 6, we illustrate the different behavior of local and global magnetization signals. Namely, we confirm that the local observable does not exhibit long-lived oscillations between local integrals of motion and it decays much more rapidly relative to the global signal. Thus, we confidently conclude that the observed time crystallinity is not induced by MBL. In Appendix D, we show that this decay is due to coherent Hamiltonian evolution by demonstrating the long-time persistence of the state when interactions are turned off. Indeed, with no interactions, the dynamics become trivial, single-spin dynamics, and we expect no difference between local and global correlations. The measured local observable under time suspension decays with a similar profile to the case of global magnetization in the noninteracting case (Fig. 2.) A more detailed discussion of the analysis of the local state under time suspension can be found in Appendix D. With this evidence in hand, we can conclusively confirm that the blue region of Fig. 5 is indeed time crystalline, for driving frequencies not too small.

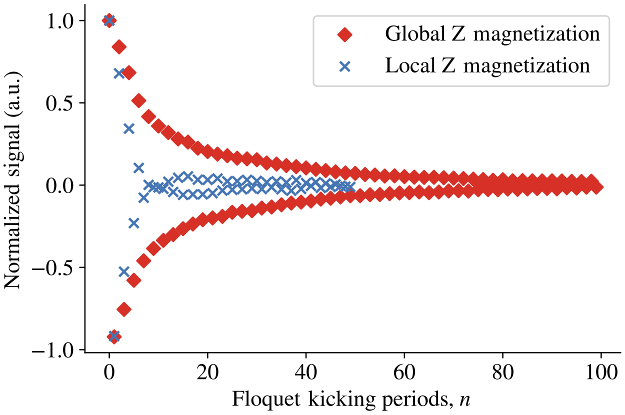

FIG. 6. Decay of local and global magnetization signals for $\theta = 170°$ kicking with $\gamma = \pi/8$ ($u = 0.1$.) The locally magnetized spin signal decays much more rapidly than the global one, as local magnetization is not conserved by the prethermal Hamiltonian. Furthermore, there is no oscillatory behavior outside of period doubling, indicating that eigenstates compatible with MBL are induced. As usual, a Floquet period corresponds to 120 μs of real-time evolution.

The rapid decay of local magnetization further solidifies the notion that, under time-crystalline evolution, short-range correlated states evolve into long-range correlated states. This is evidenced by the fact that our global magnetization signal at long times must be dominated by nonlocal correlations since $S_{\mathrm{loc}}(t) \to 0$ faster than $S(t)$, and thus the longer-lived signal,

$$S(t) - S_{\mathrm{loc}}(t) = \sum_{i\neq j} \left\langle \hat{\sigma}_z^{(i)}(t)\hat{\sigma}_z^{(j)} \right\rangle_{\beta=0}, \tag{10}$$

is dominated by nonlocal correlations.

D. Enhancing $U(1)$ conservation

In an ideal closed system under the dipolar Hamiltonian $\hat{H}_{Dz}$, the magnetization in the z direction is exactly conserved. Further, the anticommutativity of $\exp(-i\pi\hat{S}_y)$ with $\hat{S}_z$ and commutativity of $\exp(-i\pi\hat{S}_y)$ with $\hat{H}_{Dz}$ leads to the long-lived magnetization toggling response known as period doubling. This results in the emergent $U(1)$ conservation of the effective zeroth-order two-period Floquet Hamiltonian. The emergent symmetry can be further enhanced by adding a field of strength h in the z direction, $\mathcal{H}_D = H_{Dz} + h\hat{S}_z$. Luitz *et al.* [18] have previously shown that the time-averaged effective Hamiltonian over two periods is given by

$$\hat{H}_{\mathrm{eff}} = \frac{T}{T+\epsilon}\left(\hat{H}_{Dz} + \frac{\epsilon_{\mathrm{eff}}}{T}\hat{S}_y + h_{\mathrm{eff}}\hat{S}_z\right) + O(1/\omega). \tag{11}$$

Equivalent to considering the average two-period evolution, we could have chosen to consider a toggling frame

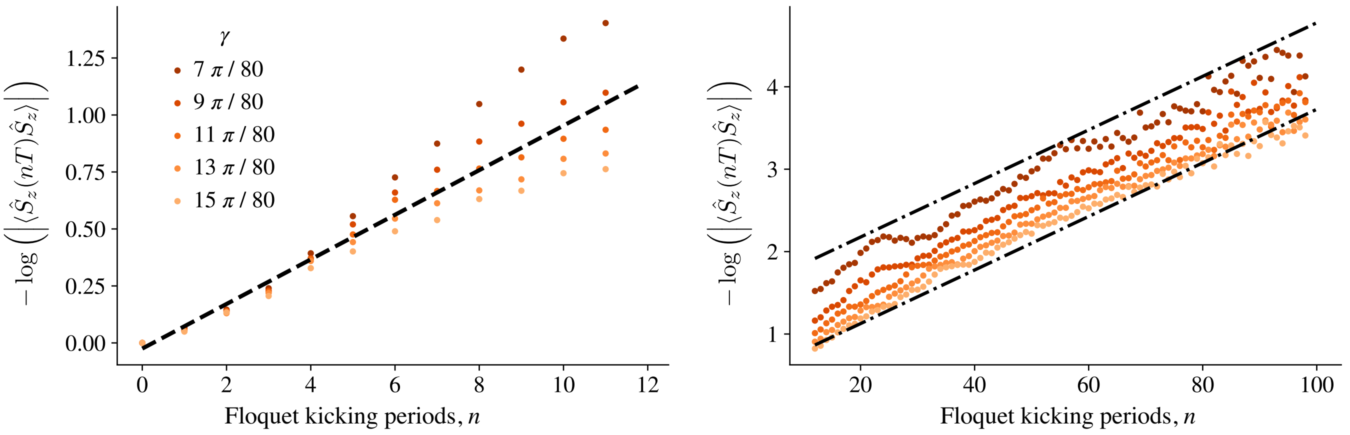

FIG. 7. Plots of the log-transformed magnetization, $-\log(|\langle \hat{S}_z(nT)\hat{S}_z|\rangle)$ as a function of Floquet kicking periods, n, for $\theta = 170°$, and select interaction magnitudes γ, in which period-doubled behavior is dominant and the driving frequency is not too slow. Notably, we see the existence of two exponential timescales shown via the linear fits in black. A short timescale, $\tau_1 \approx 7.2$ Floquet cycles (dashed line), present at early experimental times, shown on the left, gives way to a longer-lived timescale, $\tau_2 \approx 30.8$ Floquet cycles (dot-dashed line), after an initial prethermalization period, shown on the right. The partition between early and late times is made to optimize the quality of the linear fits in both regimes. As usual, a Floquet period corresponds to 120 μs of real-time evolution.

in which we undo the π rotation in each period, leaving only the ϵ rotation. Corrections to the time-averaged Hamiltonian are of order $1/\omega \sim T$. The parameters h_{eff} and ϵ_{eff} are defined via the transformation into the toggling frame of the effective two-period Hamiltonian. So long as the effective magnitude of the $\hat{S}_y$ perturbation ϵ_{eff} is small relative to the other energy scales of the Hamiltonian, namely, $h_{\text{eff}} + J_0 T_0$, the $\hat{S}_z$ magnetization is approximately conserved. The emergent $U(1)$ conservation is thus enhanced with decreasing ϵ_{eff} and increasing h_{eff}. Our phase diagram, Fig. 5, clearly demonstrates that the $U(1)$ conservation law is enhanced with decreasing ϵ at $h = 0$. It remains to demonstrate the effect of nonzero h. To this end, we introduce a stroboscopic $\hat{S}_z$ field over the Floquet period T,

$$\mathcal{H}_D = h\hat{S}_z + u\hat{H}_{D_z}, \tag{12}$$

where the maximum field possible is restricted by periodicity, so that $0 \leq hT_0 \leq \pi$, generated by a virtual-z rotation of angle hT_0 during each Floquet period. Since $[\hat{H}_{D_z}, \hat{S}_z] = 0$, there is no additional Trotter error induced by including the stroboscopic field term.

When the introduced z field takes a maximal value of $hT_0 = \pi$, we have that $h_{\text{eff}} = \epsilon_{\text{eff}} = 0$, even with $\epsilon \neq 0$. Intuitively, this result can be understood by focusing on the effects of the rotations on a single spin. During each period, the z field results in an $R_z(\pi)$ rotation that inverts the axis of the applied $R_y(\theta)$ rotation. Thus, to zeroth order, the R_y rotations cancel out, and their effect will only enter to higher order. In contrast, all other choices of $0 \leq hT_0 < \pi$ leave a finite rotation around a transverse axis, resulting in magnetization that wraps around the Bloch sphere, only returning to its origin point when $n\theta = 0 \bmod 2\pi$ (again neglecting higher-order terms in the Floquet expansion).

We repeatedly perform the experimental and fitting procedures detailed in Fig. 7 for variable $hT_0 = k\pi/4$ with $k = \{0, 1, 2, 3, 4\}$, for $\theta = 170°$. We record the results of the two-time scale fitting in Table I for each value in hT_0, making note of the γ value at which the fitting was performed. Specific fitting details are given in Appendix E in Fig. 11. We note that the two-timescale signature of prethermalization is most pronounced near the period-doubling boundary, where the timescales differ by a factor of 5 or more. This trend is consistent with the fact that the prethermal lifetime increases with increasing driving frequency, $\omega \propto 1/\gamma$. Thus, the addition of the stroboscopic z field increases the prethermal lifetime by stabilizing the time crystal at driving frequencies that would otherwise be unachievable without the addition of a z field.

Table I indicates a strong enhancement of the timescale of the prethermal regime when a z field is present. As previously developed, there are three notable regimes. The weakest conservation of $U(1)$ symmetry occurs for $hT_0 = 0$, corresponding to a prethermal timescale of about

TABLE I. Fitted timescales to prethermal $U(1)$ time-crystalline magnetization signals under a variable z field and fixed $\theta = 170°$.

hT_0	γ	τ_1 (cycles)	τ_2 (cycles)
0	$\frac{7\pi}{80}$	7.2	30.8
$\pi/4$	$\frac{\pi}{16}$	4.6	55.9
$\pi/2$	$\frac{\pi}{16}$	6.3	49.2
$3\pi/4$	$\frac{\pi}{20}$	8.7	49.8
π	$\frac{\pi}{40}$	10.6	77.5

31 Floquet cycles. The introduction of a nonzero submaximal field, $0 < hT_0 < \pi$, causes the transverse-field perturbation in the prethermal Hamiltonian to become increasingly off resonant. In these cases, the prethermal timescale is generically enhanced to around 50 Floquet cycles. At maximal field, $hT_0 = \pi$, the transverse-field perturbation is averaged out in the toggling frame, and the prethermal timescale is further enhanced to 77.5 Floquet cycles. In real-time units, this corresponds to a timescale of about 9.3 ms. The maximum-field timescale is a dramatic improvement over the zero-field timescale, as expected [18].

IV. CONCLUSION

In this work, we have demonstrated the ability to create and melt (see Fig. 5) time-crystalline order in an infinite-temperature quasi-1D nuclear spin ensemble.

The DTC behavior leads to a characteristic period-doubling response, which we analyzed by reconstructing an approximate phase diagram as a function of perturbation and driving rate. Noting, however, that the assumption that period doubling is a conclusive determinant for time crystallinity has recently been demonstrated to be false, we sought further proofs of time-crystalline order. Indeed, we note that spontaneous symmetry breaking should be forbidden in our system. First, our experimental system can be considered quasi-one dimensional and so short range, as the interchain and intrachain couplings differ by a factor of about 40. Even if the assumption that our system is an ensemble of one-dimensional spin chains fails at longer times and the dipolar interaction $1/r^3$ can then be considered long range, the high temperature still precludes time crystallinity due to prethermalization *with temperature* necessary for a SSB PDTC.

We argue instead that our system fully demonstrates “prethermalization without temperature.” Notably, we utilized a new technique to verify the fast decay of local observables to conclusively rule out stabilization due to many-body localization, such that we observe a prethermal $U(1)$ time crystal. Thanks to this insight, we further introduce a z field to successfully strengthen $U(1)$ conservation and significantly extend the time crystal’s lifetime. As proposed by Luitz *et al.*, we expect that most, if not all, high-temperature DTC studies have been instances of prethermal $U(1)$ time crystals [18]. Our work provides an accessible path towards experimental verification of prethermalization without temperature in NMR through the disordered state and observable. In particular, we believe that Rovny *et al.*’s ADP sample has sufficient disorder generated by nearby hydrogen atoms to probe local observables.

Our results also indicate that the time-crystalline phase is characterized by long-range correlations. An interesting future direction would be to try to utilize Hamiltonian engineering to perform time reversal on a time-crystalline system, as done in previous NMR DTC experiments [15,16], and thus explore generated localization lengths. In a time-crystalline system, we expect to measure rapidly growing localization lengths as the initial state evolves into a long-range spatiotemporal correlated state, in contrast to the local integrals of motion present in an MBL state.

ACKNOWLEDGMENTS

The authors would like to thank Pai Peng, Alex Ungar, and Santiago Hernández-Gómez for helpful discussions that enabled this work. This work was supported in part by the National Science Foundation under Grants No. PHY1915218 and No. PHY1734011, and the CQE-LPS Doc Bedard Fellowship.

APPENDIX A: HAMILTONIAN ENGINEERING

Within the main text, we utilized two central Hamiltonian engineering sequences, Wei16 and Peng24. Wei16 is a 16-pulse sequence, composed of four similarly structured four-pulse blocks [29]. Unless otherwise specified, a pulse corresponds to a $\pi/2$ rotation about a particular transverse axis of the Bloch sphere obtained by turning on the rf driving for $t_p = 1.02$ μs. Each four-pulse block corresponds to $6\tau_0$ of time, where $\tau_0 = 5$ μs is the delay primitive for the entire sequence. It is prudent to choose τ_0 to be as short as possible in order to minimize Trotter errors while still ensuring that interpulse delays $\tau_0 - t_p$ are not too short. For our spectrometer, $\tau_0 = 5$ μs is as short as feasible, given that the electronics require a minimum pulse separation of 2.5 μs to change the phase for the next applied pulse. Under Wei16, the internal Hamiltonian given in Eq. (1) can be transformed to a model with six free parameters—three controlling the interaction Hamiltonian and three controlling the orientation of the local field. Notably, with collective rotations, we cannot change the sum of the coefficients of the interaction Hamiltonian since the subspace generated by the dipolar interaction along x, y, and z, written $\mathrm{span}\{\mathcal{H}_{D_x}, \mathcal{H}_{D_y}, \mathcal{H}_{D_z}\}$, is a two-dimensional vector space. This can be seen clearly by recalling one of the central identities used to perform time suspension, $\mathcal{H}_{D_x} + \mathcal{H}_{D_y} + \mathcal{H}_{D_z} = 0$. The constraint is directly captured in the Floquet Hamiltonian defined as

$$\mathcal{H}_F = \frac{1}{2}\sum_{i<j} J_{ij}\Big((u-w)\hat{S}_x^{(i)}\hat{S}_x^{(j)} + (v-u)\hat{S}_y^{(i)}\hat{S}_y^{(j)} + (w-v)\hat{S}_z^{(i)}\hat{S}_z^{(j)} \Big) + \frac{1}{3}\sum_i \omega_i \Big(a\hat{S}_x^{(i)} + b\hat{S}_y^{(i)} + c\hat{S}_z^{(i)} \Big). \tag{A1}$$

$$\begin{aligned}&\tau_1 = \tau_0(1+c-v+w), \qquad \tau_2 = \tau_0(1+b-u+v),\\&\tau_3 = \tau_0(1-a+u-w),\\&\tau_1' = \tau_0(1-c-v+w), \qquad \tau_2' = \tau_0(1-b-u+v),\\&\tau_3 = \tau_0(1+a+u-w).\end{aligned}\tag{A2}$$

Each of the parameters appearing above are combined to produced the physical pulse delays for the sequence. In general, a four-pulse sequence is defined by five delays and four orientations, which we collect using the following notation: $P(t_1, \boldsymbol{n}_1, t_2, \boldsymbol{n}_2, t_3, \boldsymbol{n}_3, t_4, \boldsymbol{n}_4, t_5)$, a standard notation for our group [21,29]. Unlike strings of unitary operators, this notation is read from left to right, in the order they are physically applied during an experiment. Namely, the generic pulse sequence corresponds to "wait for t_1, then apply a pulse in the $\boldsymbol{n}_1$ direction, then wait for t_2, …" and so on. Concretely, the Wei16 sequence is given by the string of four pulse blocks shown in Eq. (A3). We use the standard notation $\bar{\boldsymbol{x}} = -\boldsymbol{x}$, which helps save horizontal space. In this sequence, there is a great deal of reflection symmetry. Generally, symmetrized pulse sequences perform better than their unsymmetrized counterparts, which can be formalized by computing leading-order error terms.

The Peng24 sequence differs from Wei16 in that it is constructed by symmetrizing a pulse sequence reliant on a threefold symmetry, which differs significantly from the usual twofold-symmetry four-pulse blocks demonstrated above. Additionally, as a time-suspension sequence, the target Hamiltonian is much simpler, $\mathcal{H}_F = 0$. In particular, we chose Peng24, as it is a 24-pulse sequence corresponding to $24\tau_0$ of evolution time, equivalent to that of Wei16, allowing for a direct comparison. We can write Peng24 in the same way as we wrote Wei16, taking the standard pulse block to include three orientations and four delays in order to better emphasize the symmetry group. Since Peng24 is the symmetrized Angle12, we define Angle12 in Eq. (A4) and solidify how it is used to define Peng24 (first introduced as $yxx24$) [31].

$$P(\tau_1,\boldsymbol{x},\tau_2,\boldsymbol{y},2\tau_3,\boldsymbol{y},\tau_2',\boldsymbol{x},\tau_1')P(\tau_1',\boldsymbol{x},\tau_2,\boldsymbol{y},2\tau_3',\boldsymbol{y},\tau_2',\boldsymbol{x},\tau_1)P(\tau_1,\bar{\boldsymbol{x}},\tau_2',\bar{\boldsymbol{y}},2\tau_3',\bar{\boldsymbol{y}},\tau_2,\bar{\boldsymbol{x}},\tau_1')P(\tau_1',\bar{\boldsymbol{x}},\tau_2',\bar{\boldsymbol{y}},2\tau_3,\bar{\boldsymbol{y}},\tau_2,\bar{\boldsymbol{x}},\tau_1),\tag{A3}$$

$$\text{Angle12} = P\left(\frac{\tau_0}{2},\bar{\boldsymbol{y}},\tau_0,\boldsymbol{x},\tau_0,\bar{\boldsymbol{x}},\frac{\tau_0}{2}\right)P\left(\frac{\tau_0}{2},\boldsymbol{y},\tau_0,\bar{\boldsymbol{x}},\tau_0,\bar{\boldsymbol{x}},\frac{\tau_0}{2}\right)P\left(\frac{\tau_0}{2},\bar{\boldsymbol{y}},\tau_0,\boldsymbol{x},\tau_0,\bar{\boldsymbol{x}},\frac{\tau_0}{2}\right)P\left(\frac{\tau_0}{2},\boldsymbol{y},\tau_0,\boldsymbol{x},\tau_0,\boldsymbol{x},\frac{\tau_0}{2}\right).\tag{A4}$$

As stated, Peng24 is formed by symmetrizing Angle12, which is done by performing Angle12, followed by $\overline{\text{Angle12}}$. The overbar on Angle12 means to perform Angle12, albeit with the signs of each pulse orientation reversed, $\boldsymbol{x} \to \bar{\boldsymbol{x}}$, etc. Hence, Peng24 = $\text{Angle12}\overline{\text{Angle12}}$.

APPENDIX B: RANDOM-STATE GENERATION

The procedure for generating the random state, and thus local observables in NMR, was first introduced by Peng *et al.* on this experimental platform [21]. Extensive details on the generation of random Zeeman states and random double-quantum states, along with a discussion and verification of their properties, can be found in the Supplemental Material [40]. Here, we reproduce some of the details relevant to our experiments, particularly the generation of random Zeeman states.

The goal is to find a unitary operator that maps our initial state to the disordered state,

$$\hat{U}_d\colon\ \hat{S}_z \to \sum_i \xi_i \hat{S}_z^{(i)},\tag{B1}$$

generated only using collective rotations. This is possible due to the local field generated by the heteronuclear interaction of our fluorine chain with nearby phosphorus atoms,

$$\mathcal{H}_{\text{dis}} = \sum_{i,j} J_{ij}^{FP} \hat{S}_z^{(i)} \hat{I}_z^{(j)} \approx \sum_i \omega_i \hat{S}_z^{(i)}.\tag{B2}$$

The Zeeman polarization of the phosphorus spin, $\hat{I}_z^{(i)}$, is well approximated as a classical random variable that takes values of ± 0.5 with equal probability. Over the timescale of a given experiment, the state of a given phosphorus spin is approximately fixed, so the interaction is a source of quenched disorder. To make use of the disordered field, we turn off the dipolar interaction using a well-known spectral sequence, WAHUHA8. The WAHUHA sequence [28] is a four-pulse decoupling sequence, which we symmetrize to form the eight-pulse sequence WAHUHA8:

$$\begin{aligned}\text{WAHUHA8} = {}& P(\tau_0,\boldsymbol{x},\tau_0,\boldsymbol{y},2\tau_0,\bar{\boldsymbol{y}},\tau_0,\bar{\boldsymbol{x}},\tau_0)\\&\times P(\tau_0,\bar{\boldsymbol{x}},\tau_0,\bar{\boldsymbol{y}},2\tau_0,\boldsymbol{y},\tau_0,\boldsymbol{x},\tau_0).\end{aligned}\tag{B3}$$

In addition to decoupling the dipolar interaction of the fluorine atoms, WAHUHA8 leaves the disordered-field orientation unchanged, with a resulting Floquet Hamiltonian of

$$\mathcal{H}_{WHH} = \frac{1}{3}\sum_i h_i \hat{S}_z^{(i)} = \sum_i \omega_i \hat{S}_z^{(i)}.\tag{B4}$$

Other eight-pulse spectral sequences can alter the orientation of the disordered field, such as MREV-8 [27], which is undesirable for this procedure.

The final ingredient needed to construct $\hat{U}_d$ is phase cycling, an NMR technique in which multiple experimental signals are added (or subtracted) together in order to cancel unwanted terms generated during evolution. All data within the main text used phase cycling to reduce systemic sources of noise generated by experimental imperfections and electronic control error. With this in mind, we present the procedure for generating random Zeeman states below.

(1) The state is initialized via thermalization by waiting $5T_1$, so $\delta\rho_1 = \hat{S}_z$.

(2) The state is rotated by a pulse along the $\boldsymbol{y}$ axis, so $\delta\rho_2 = \hat{S}_x$. The state no longer commutes with the disordered field and will begin to evolve.

(3) Immediately following the previous step, the WAHUHA8 sequence is performed 18 times in a row, corresponding to $\tau_d = 60\tau_0 \times 18 = 1.08$ ms of total evolution under the disordered Hamiltonian. The resulting state is then $\delta\rho_3 = \sum_i \cos(\omega_i \tau_d)\hat{S}_x^{(i)} + \sin(\omega_i \tau_d)\hat{S}_y^{(i)}$.

(4) To get the disordered phase tagging along $\hat{S}_z^{(i)}$, a $\pi/2$ rotation is performed about the $\boldsymbol{x}$ or $\boldsymbol{y}$ axis. The choice is arbitrary as long as it is consistent; it will be clear that this choice determines whether the phase tagging is the sine or cosine of the disordered field. As an odd function, the choice of sine over cosine ensures the random phase tagging is zero mean even in the presence of finite temperatures. In this and previous works, $\boldsymbol{x}$ is chosen, leading to the state $\delta\rho_4^{(1)} = \sum_i \cos(\omega_i \tau_d)\hat{S}_x^{(i)} - \sin(\omega_i \tau_d)\hat{S}_z^{(i)}$. Twofold phase cycling on the sign of the $\boldsymbol{x}$ pulse is performed. The first state is subtracted from another state generated by following steps (1)–(3), finally performing a $\bar{\boldsymbol{x}}$ pulse resulting in $\delta\rho_4^{(2)} = \sum_i \cos(\omega_i \tau_d)\hat{S}_x^{(i)} + \sin(\omega_i \tau_d)\hat{S}_z^{(i)}$. The subtraction of these states yields the desired result: $\delta\rho_4 = \delta\rho_4^{(2)} - \delta\rho_4^{(1)} \propto \sum_i \sin(\omega_i \tau_d)\hat{S}_z^{(i)}$.

(5) Finally, a fourfold phase cycling is performed to reduce systematic error. The initial and final states resulting from steps (1)–(4) are entirely unchanged if *all* pulses are shifted in phase by 90 degrees. Including this phase-cycling step reduces error and leads to a larger signal, resulting in a procedure that requires an eightfold phase cycling to generate $\hat{U}_d$.

We have given a procedure for generating the random Zeeman state from the initial thermal state. The procedure to generate the random Zeeman observable is precisely the procedure used to generate the random Zeeman state, albeit in reverse. Following steps (1)–(5) in reverse will engineer $\hat{U}_d^\dagger$, leading to the desired observable. However, this procedure would require $8 \times 8 = 64$-fold phase cycling, so each data point would take 4.25 minutes to acquire and would include a significant amount of noise. In engineering $\hat{U}_d^\dagger$, we omit the fourfold phase cycling detailed in step (5), so we only need to perform a 16-fold phase cycle. It has previously been argued that, under certain circumstances, the number of scans required can be reduced further [21]. For all experimental data shown in the text involving local observables, 16-fold phase cycling is used.

APPENDIX C: FITTING TO PERIOD-DOUBLED DECAYS, VARIABLE INTERACTION TIME

Here, we detail the fitting procedure to the period-doubled response under time-crystalline driving, where the interaction period is variable. The model of interest is a stretched exponential function with four parameters,

$$S(t) = a\exp\left(-(t/\tau)^b\right) + c, \tag{C1}$$

previously introduced in this work in Eq. (7). The fitting is performed in Python using SciPy's `curve_fit` function [41]. We consider $T \in \{15, 30, 45, 60, 90, 120\}$ μs, which corresponds to dimensionless interaction magnitudes $\gamma \in \{5\pi/32, 5\pi/16, 15\pi/32, 5\pi/8, 15\pi/16, 5\pi/4\}$. The results are shown in Fig. 8.

In Fig. 8, there are two points of note. First, the fitting for $T = 15$ μs (left plot) shows a systematic error: The model is a bad fit for the given data. In this case, the two-timescale fitting procedure is a better choice, and it matches the notion that high driving frequency leads to prethermal time crystallinity. As we continue to increase the Floquet period T, we similarly argue that the two-timescale fitting procedure is a bad choice. In Fig. 9, we show the results of the two-timescale fitting procedure for $T = 15, 30$ μs. The $T = 15$ fitting demonstrates a strongly resolved transition between timescales; the $T = 30$ plot indicates that there might be a second timescale, but the transition between prethermalizing and prethermal timescales is weak. Notably, the choice of the cutting point between timescales does not significantly impact the fitting results. Hence, the argument in favor of prethermalization is quite weak, so we take the single stretched-exponential fit to be sufficiently explanatory. Second, while there is a clear and apparent increase in the signal lifetime as the kicking period T increases, we recall that this corresponds to *decreasing* ω. In the limit of increasing ω, we expect that the dynamics are not prethermal; rather, they are decoherence dominated. When analyzing the lifetime dependency as a function of the driving period, we notice that τ is a linearly increasing function of the driving period T in this regime, demonstrated in Fig. 8 (right). The linear trend, $37.11T - 453.39$ (μs), can be expressed in terms of the number of periods by dividing by the driving period T, becoming $\tau_F(T) = 37.11–453.39/T$ (periods).

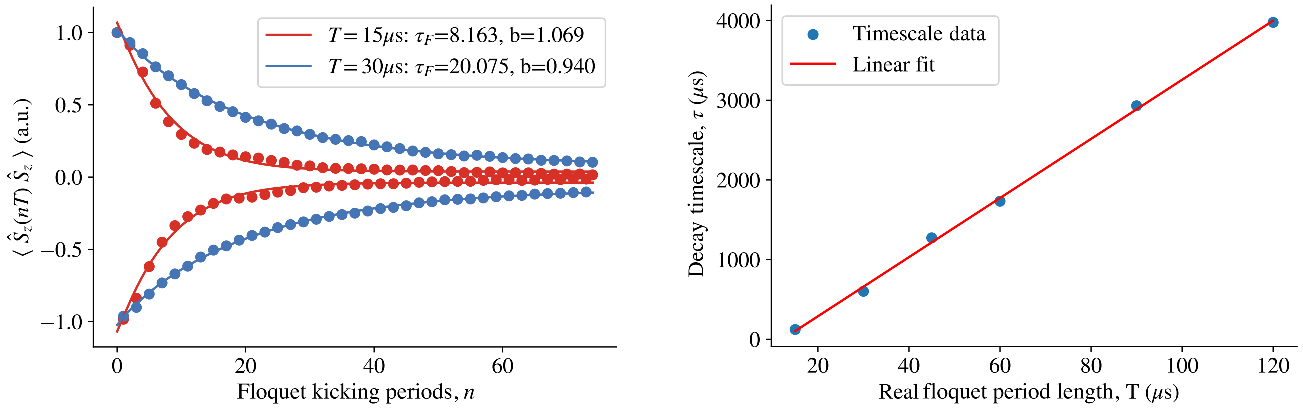

FIG. 8. Left panel: exemplary fitting results for variable interaction-time DTC experiments, plotted in nondimensional Floquet periods instead of evolution time for a more uniform comparison. For each fit, the relevant extracted parameters are the nondimensional decay timescale $\tau_F = \tau/T$ (units of Floquet periods) and the exponential stretching parameter b. Right panel: interpolation of the signal lifetimes extracted from fittings as shown on the left panel, as a function of the Floquet period T, $\tau(T) = aT - b$. The fitted parameters are $a = 37.11$ (nondimensional) and $b = 453.39$ μs.

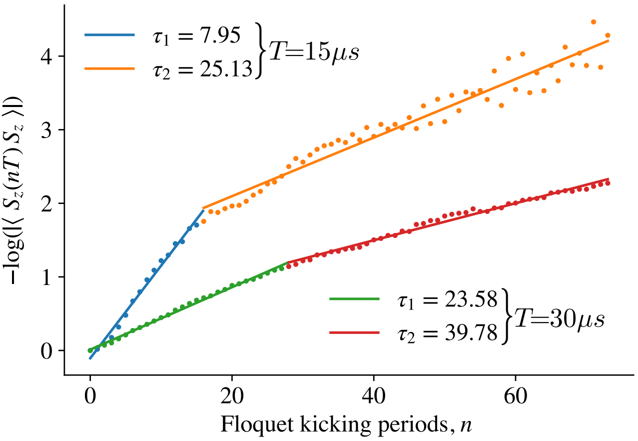

FIG. 9. Two-timescale fitting for the $T = 15$ μs DTC experiment and the $T = 30$ μs DTC experiment in nondimensional units of Floquet periods.

This expression highlights that there is an apparent upper bound to the lifetime of the signal, 37.11 Floquet periods. Thus, we have evidence that the dynamics for experiments in which γ is too large are decoherence dominated and not prethermal. Then, the period-doubling dynamics are trivially generated by decoherence and not time crystalline. Conversely, when γ is too small, the time crystal melts, and period doubling fails. Determining the transition point between prethermal time-crystalline dynamics and decoherence-dominated dynamics would require defining a suitable witness for cleanly differentiating between these modalities, beyond the analysis we performed above.

APPENDIX D: LOCAL Z-MAGNETIZATION STATE MANIPULATIONS

In order to further verify our ability to produce a robust local state, we consider the case where interactions are turned off entirely. Indeed, we want to ensure that the rapid decay observed in Fig. 6 is due to time-crystal-inducing interactions and not due to poor state preparation. In Fig. 10, we demonstrate that the local magnetization signal

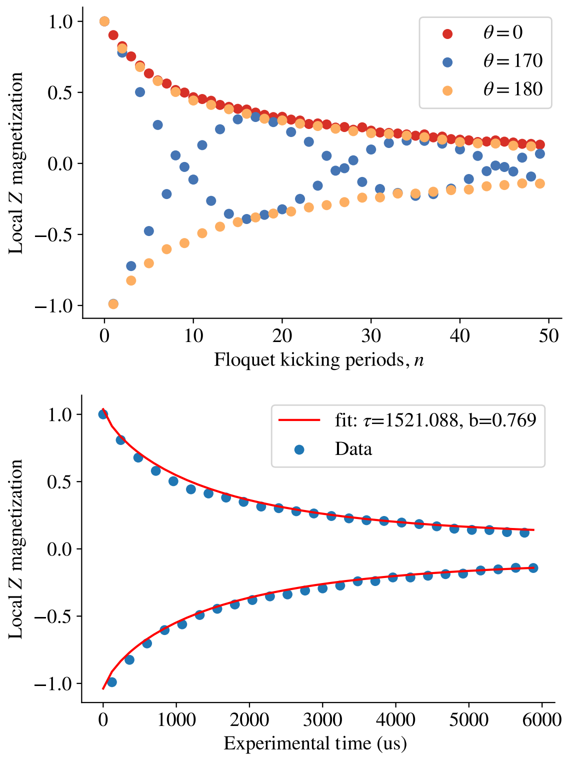

FIG. 10. Results of local z state experiments under periodic driving with interactions turned off via Peng24. In the top panel, signals are shown for kicking angles $\theta = 0°, 170°, 180°$. We notice that the decay envelope is similar for all three cases, as in the global z case, albeit decaying more rapidly. In the bottom panel, we show the fitting of the $\theta = 180°$ signal to the four-parameter model given in Eq. (7).

persists for long times when interactions are turned off with Peng24. In fact, the observed decay envelope fits well to the four-parameter model of Eq. (7), with a sublinear exponential argument similar to the noninteracting global magnetization response. The timescale of the decay is shorter for the local magnetization than global magnetization, $\tau = 1.5$ ms, as compared to the 6.5-ms decay timescale for the global observable, shown in Fig. 2. Importantly, this is still quite long compared to $T_2 \approx 30$ μs.

It is also important to note that our ability to transfer population from the disordered state back to a directly measurable observable is predicated on the disorder being fixed over the timescale of a single experiment. Namely, if the disordered field has changed significantly as a result of the flipping of nearby phosphorus spins, then we would see a complete loss of signal upon measuring. We expect that the timescale of variation for the phosphorus spins is generated by spin diffusion or by a T_1 process. In either case, we believe that the timescale is quite long, given that we are able to refocus the disordered state after over 6 ms of evolution under a time-suspension sequence. The decay timescale measured, $\tau = 1.5$ ms, reflects decay due to both Trotter errors in the time-suspension sequence and refocusing errors due to the disordered-field variation. Naively assuming additive rates and identical noise processes, we can estimate the timescale of disorder variation to be $\tau_P \approx (1/1.5 - 1/6.5)^{-1} = 1.95$ ms. In summary, the results of Fig. 10 demonstrate that our state preparation procedure and control scheme are not the causes of the rapid decay seen in Fig. 6.

APPENDIX E: TWO-TIMESCALE FITTING RESULTS, VARIABLE INTERACTION STRENGTH

In Fig. 11, we show the two-timescale fitting results for stroboscopic z-field strengths of $hT = \pi/2, \pi$. This fitting procedure is performed for all $hT \in \{\pi/4, \pi/2, 3\pi/4, \pi\}$ to populate Table I. The fitting for $hT = 0$ is shown in Fig. 7. Concretely, τ_1 gives the decay timescale of the initial state to the prethermal time-crystalline state, and τ_2 gives the lifetime of the prethermal time-crystalline state.

For each value of hT, an optimal γ is selected to maximize the two-timescale contrast. Generally, for larger values of hT, smaller values of γ are used. For a prethermal time crystal, τ_2 is expected to depend exponentially on γ. We notice the symptoms of this effect in that the quality of the fit is increasingly sensitive to large changes in γ with increasing hT. Unfortunately, direct analysis of this exponential growth is not feasible on our system. First, in the limit $\omega \to \infty$, $\gamma \to 0$, our signal will still decay due to various decoherence and Hamiltonian engineering effects. Second, we have demonstrated that decreasing γ below the phase boundary melts the time-crystalline order. It would be interesting to consider taking γ to be arbitrarily close to the phase boundary; however, we lack the control resolution to explore this regime.

The fitting in Fig. 7 shows that the prethermal timescale is robust to changes in γ, which can be attributed to the fact that the transition to the time-crystalline phase occurs near $\gamma = (7\pi/80)$. Thus, $\Delta\gamma = (\pi/40)$ is a small fraction of the interaction magnitude at the transition point. Even so, the contrast between timescales is most pronounced for $\gamma = (7\pi/80)$. However, for $hT = \pi$, the transition point to the time-crystalline phase occurs near $\gamma = \pi/40 (u = 0.02)$. Given our resolution in γ is limited to $\pi/80$, we are limited to (proportionally) large changes in the interaction magnitude relative to the transition point. If our timing control allowed for a higher resolution in u, then we could reconstruct a phase diagram for each hT similar to Fig. 5. Qualitatively, we expect the transition boundary to be "pushed down" with increasing hT, increasing the phase-space area occupied by the time-crystalline state. Most notably, this allows for exploring smaller values of γ, hence larger ω, while maintaining time crystallinity, thus allowing for further exploration of the predicted exponential dependency on ω.

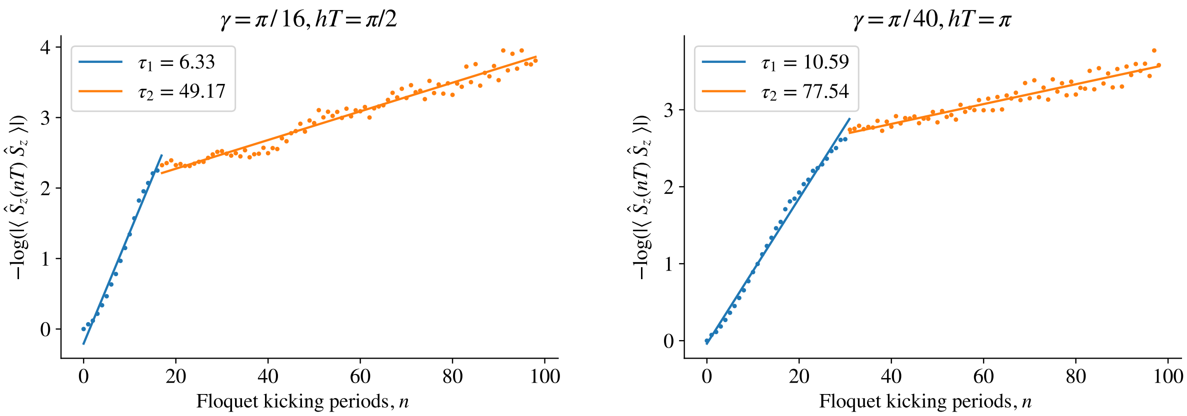

FIG. 11. Two-timescale fitting results for various applied stroboscopic z fields, in nondimensional units of Floquet periods. The data generated by this procedure are used to populate the entries of Table I.

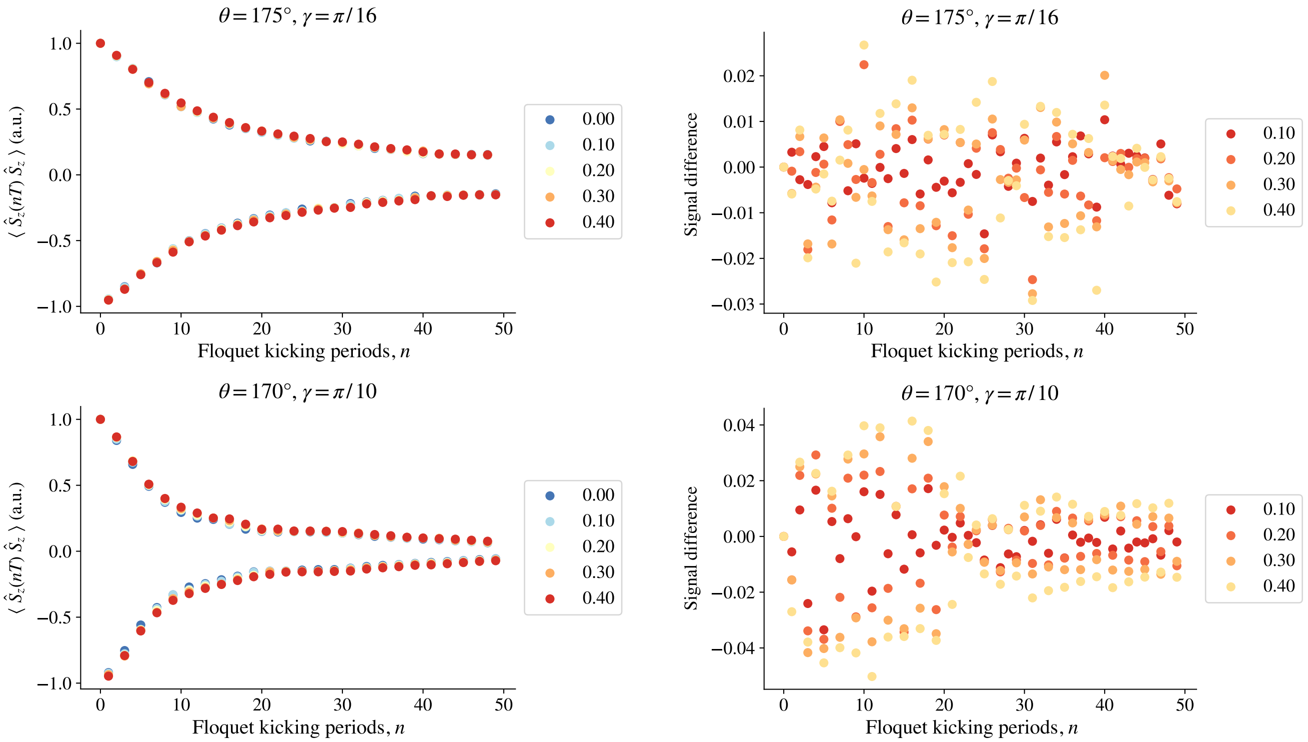

FIG. 12. Effects of increasing disorder on time crystallinity for $\theta = 175°$, $\gamma = \pi/16$, and $\theta = 170°$, $\gamma = \pi/8$. On the left, we show the measured magnetization signal for each instance of scaled disorder strength, $v \in \{0.0, 0.1, 0.2, 0.3, 0.4\}$. Here, v multiplies the disordered field in the Floquet engineered Hamiltonian as generated by Wei16. The Hamiltonian for variable v is given in Eq. (F1). On the right, we take the difference between experiments with disorder and experiments with no disorder. Notice that the disordered field does not stabilize the signal; increasing disorder simply leads to increased variability in the measured signal.

APPENDIX F: EFFECTS OF DISORDERED FIELDS

Using Wei16, we can vary the effective disorder strength over a single Floquet period. Concretely, we have two tunable parameters, u, v, such that our Floquet Hamiltonian is

$$\hat{H}_F = \frac{v}{3}\sum_i \omega_i \hat{\sigma}_z^{(i)} + \frac{u}{2}\sum_{i<j} J_0\left(\hat{S}_z^{(i)}\hat{S}_z^{(j)} - \frac{1}{2}\left(\hat{S}_x^{(i)}\hat{S}_x^{(j)} + \hat{S}_y^{(i)}\hat{S}_y^{(j)}\right)\right). \tag{F1}$$

Above, ω_i is the locally disordered field induced by the unpolarized phosphorus spins, and $0 \leq v \leq 0.4$ is the allowed parameter range under Wei16. Then, for selected kicking angles θ and interaction strengths γ, we can investigate the effect of disorder on the stability of our time crystal. The results of this investigation are given in Fig. 12. In summation, we see no evidence that increasing disorder leads to a longer-lived signal; hence, MBL is likely not the stabilization mechanism for this time crystal.

[1] F. Wilczek, *Quantum time crystals*, Phys. Rev. Lett. **109**, 160401 (2012).

[2] P. Bruno, *Impossibility of spontaneously rotating time crystals: A no-go theorem*, Phys. Rev. Lett. **111**, 070402 (2013).

[3] D. V. Else, B. Bauer, and C. Nayak, *Prethermal phases of matter protected by time-translation symmetry*, Phys. Rev. X **7**, 011026 (2017).

[4] J. Zhang, P. W. Hess, A. Kyprianidis, P. Becker, A. Lee, J. Smith, G. Pagano, I.-D. Potirniche, A. C. Potter, A. Vishwanath *et al.*, *Observation of a discrete time crystal*, Nature (London) **543**, 217 (2017).

[5] M. Ippoliti, K. Kechedzhi, R. Moessner, S. Sondhi, and V. Khemani, *Many-body physics in the NISQ era: Quantum programming a discrete time crystal*, PRX Quantum **2**, 030346 (2021).

[6] X. Mi, M. Ippoliti, C. Quintana, A. Greene, Z. Chen, J. Gross, F. Arute, K. Arya, J. Atalaya, R. Babbush *et al.*, *Time-crystalline eigenstate order on a quantum processor*, Nature (London) **601**, 531 (2022).

[7] A. Lazarides and R. Moessner, *Fate of a discrete time crystal in an open system*, Phys. Rev. B **95**, 195135 (2017).

[8] F. Machado, D. V. Else, G. D. Kahanamoku-Meyer, C. Nayak, and N. Y. Yao, *Long-range prethermal phases of nonequilibrium matter*, Phys. Rev. X **10**, 011043 (2020).

[9] J. Berges, S. Borsányi, and C. Wetterich, *Prethermalization*, Phys. Rev. Lett. **93**, 142002 (2004).

[10] T. Mori, T. N. Ikeda, E. Kaminishi, and M. Ueda, *Thermalization and prethermalization in isolated quantum systems: A theoretical overview*, J. Phys. B **51**, 112001 (2018).

[11] A. Kyprianidis, F. Machado, W. Morong, P. Becker, K. S. Collins, D. V. Else, L. Feng, P. W. Hess, C. Nayak, G. Pagano *et al.*, *Observation of a prethermal discrete time crystal*, Science **372**, 1192 (2021).

[12] W. Beatrez, C. Fleckenstein, A. Pillai *et al.*, *Critical prethermal discrete time crystal created by two-frequency driving*, Nat. Phys. **19**, 407 (2023).

[13] P. Frey and S. Rachel, *Realization of a discrete time crystal on 57 qubits of a quantum computer*, Sci. Adv. **8**, eabm7652 (2022).

[14] S. Choi, J. Choi, R. Landig, G. Kucsko, H. Zhou, J. Isoya, F. Jelezko, S. Onoda, H. Sumiya, V. Khemani *et al.*, *Observation of discrete time-crystalline order in a disordered dipolar many-body system*, Nature (London) **543**, 221 (2017).

[15] J. Rovny, R. L. Blum, and S. E. Barrett, *P-31 NMR study of discrete time-crystalline signatures in an ordered crystal of ammonium dihydrogen phosphate*, Phys. Rev. B **97**, 184301 (2018).

[16] J. Rovny, R. L. Blum, and S. E. Barrett, *Observation of discrete-time-crystal signatures in an ordered dipolar many-body system*, Phys. Rev. Lett. **120**, 180603 (2018).

[17] D. V. Else, C. Monroe, C. Nayak, and N. Y. Yao, *Discrete time crystals*, Annu. Rev. Condens. Matter Phys. **11**, 467 (2020), 10.1146/annurev-conmatphys-031119-050658.

[18] D. J. Luitz, R. Moessner, S. L. Sondhi, and V. Khemani, *Prethermalization without temperature*, Phys. Rev. X **10**, 021046 (2020).

[19] M. Collura, A. De Luca, D. Rossini, and A. Lerose, *Discrete time-crystalline response stabilized by domain-wall confinement*, Phys. Rev. X **12**, 031037 (2022).

[20] P. Peng, *Prethermalization and localization in quantum spin chains*, Ph.D. thesis, Massachusetts Institute of Technology (2019).

[21] P. Peng, B. Ye, N. Y. Yao, and P. Cappellaro, *Exploiting disorder to probe spin and energy hydrodynamics* (2022).

[22] L. S. Martin, H. Zhou, N. T. Leitao, N. Maskara, O. Makarova, H. Gao, Q.-Z. Zhu, M. Park, M. Tyler, H. Park, S. Choi, and M. D. Lukin, *Controlling local thermalization dynamics in a floquet-engineered dipolar ensemble* (2022).

[23] N. Leroy, E. Bres, D. Jones, and S. Downes, *Structure and substitutions in fluorapatite*, Eur. Cells Mater. **2**, 36 (2001).

[24] W. Zhang, P. Cappellaro, N. Antler, B. Pepper, D. G. Cory, V. V. Dobrovitski, C. Ramanathan, and L. Viola, *NMR multiple quantum coherences in quasi-one-dimensional spin systems: Comparison with ideal spin-chain dynamics*, Phys. Rev. A **80**, 052323 (2009).

[25] E. Knill, R. Laflamme, R. Martinez, and C.-H. Tseng, *An algorithmic benchmark for quantum information processing*, Nature (London) **404**, 368 (2000).

[26] D. C. McKay, C. J. Wood, S. Sheldon, J. M. Chow, and J. M. Gambetta, *Efficient Z gates for quantum computing*, Phys. Rev. A **96**, 022330 (2017).

[27] P. Mansfield, M. J. Orchard, D. C. Stalker, and K. H. B. Richards, *Symmetrized multipulse nuclear-magnetic-resonance experiments in solids: measurement of the chemical-shift shielding tensor in some compounds*, Phys. Rev. B **7**, 90 (1973).

[28] J. Waugh, L. Huber, and U. Haeberlen, *Approach to high-resolution NMR in solids*, Phys. Rev. Lett. **20**, 180 (1968).

[29] K. X. Wei, C. Ramanathan, and P. Cappellaro, *Exploring localization in nuclear spin chains*, Phys. Rev. Lett. **120**, 070501 (2018).

[30] C. M. Sánchez, A. K. Chattah, K. X. Wei, L. Buljubasich, P. Cappellaro, and H. M. Pastawski, *Perturbation independent decay of the Loschmidt echo in a many-body system*, Phys. Rev. Lett. **124**, 030601 (2020).

[31] P. Peng, X. Huang, C. Yin, L. Joseph, C. Ramanathan, P. Cappellaro, *Deep reinforcement learning for quantum Hamiltonian engineering*, Phys. Rev. Appl. **18**, 024033 (2022).

[32] T.-S. Zeng and D. N. Sheng, *Prethermal time crystals in a one-dimensional periodically driven floquet system*, Phys. Rev. B **96**, 094202 (2017).

[33] A. Pizzi, J. Knolle, and A. Nunnenkamp, *Higher-order and fractional discrete time crystals in clean long-range interacting systems*, Nat. Commun. **12**, 1 (2021).

[34] G. Giachetti, A. Solfanelli, L. Correale, and N. Defenu, *High-order time crystal phases and their fractal nature* (2022).

[35] G. S. Boutis, D. Greenbaum, H. Cho, D. G. Cory, and C. Ramanathan, *Spin diffusion of correlated two-spin states in a dielectric crystal*, Phys. Rev. Lett. **92**, 137201 (2004).

[36] W. Zhang and D. G. Cory, *First direct measurement of the spin diffusion rate in a homogenous solid*, Phys. Rev. Lett. **80**, 1324 (1998).

[37] P. Peng, Z. Li, H. Yan, K. X. Wei, P. Cappellaro, *Comparing many-body localization lengths via nonperturbative construction of local integrals of motion*, Phys. Rev. B **100**, 214203 (2019).

[38] M. Serbyn, Z. Papić, and D. A. Abanin, *Local conservation laws and the structure of the many-body localized states*, Phys. Rev. Lett. **111**, 127201 (2013).

[39] M. Serbyn, Z. Papić, and D. A. Abanin, *Quantum quenches in the many-body localized phase*, Phys. Rev. B **90**, 174302 (2014).

[40] See Supplemental Material at http://link.aps.org/supplemental/10.1103/PhysRevX.13.041016 for details.

[41] P. Virtanen, R. Gommers, T. E. Oliphant, M. Haberland, T. Reddy, D. Cournapeau, E. Burovski, P. Peterson, W. Weckesser, J. Bright *et al.*, and SciPy1.0 contributors, *SciPy1.0: Fundamental algorithms for scientific computing in PYTHON*, Nat. Methods **17**, 261 (2020).